International Journal of Solids and Structures 47 (2010) 2143–2154

Contents lists available at ScienceDirect

International Journal of Solids and Structures

journal homepage: www.elsevier.com/locate/ijsolstr

Vibration and stability of a constrained elastica with variable length

Wei-Chia Ro, Jen-San Chen *, Shau-Yu Hong

Department of Mechanical Engineering, National Taiwan University, Taipei 10617, Taiwan

ARTICLE INFO

Article history:
Received 10 November 2009
Received in revised form 9 April 2010
Available online 21 April 2010

Keywords:
Constrained elastica
Vibration
Stability
Plane walls
Load control

ABSTRACT

This paper studies the vibration and stability of an elastica constrained by a pair of symmetrically placed parallel plane walls. One end of the elastica is fully clamped, while the other end is allowed to slide through a rigid channel under edge thrust. In order to take into account the variation of the contact points between the elastica and the walls during vibration, an Eulerian version of the equations of motion is adopted. It is found that the lowest few natural frequencies approach and remain degenerately zero when point-contact deformations evolve to line-contact patterns. As a consequence, the stability of all line-contact deformations before secondary buckling cannot be determined from the linear vibration analysis. A load-controlled experiment was conducted to find that the elastica jumped from one-point to two-point, and then to three-point contact with the walls without going through any line-contact deformations. These experimental observations are different from the results reported previously by others with different set-ups, in which line-contact deformations did exist. Explanations based on experimental evidences and theoretical analyses are provided to confirm the validity of these previous investigations and clarify the cause of the difference.

© 2010 Elsevier Ltd. All rights reserved.

1. Introduction

The primary goal of the research in constrained elastica is to understand the behavior of a thin elastic strip under edge thrust when it is subject to lateral surface constraints. It finds applications in a variety of practical problems, such as in compliant foil journal bearings, corrugated fiberboard, deep drilling, structural core sandwich panels, sheet forming, non-woven fabrics manufacturing, and stent deployment procedures. By assuming small deformation, Feodosyev (1977) included the problem of a pinned–pinned buckled beam constrained by a pair of parallel walls as an exercise for a university strength and material course. Adan et al. (1994) showed that when a column with initial imperfection positioned at a distance from a plane wall is subject to compression, contact zones may develop leading to buckling mode transition. Domokos et al. (1997) and Chai (1998, 2002) investigated the planar buckling patterns of an elastica constrained inside a pair of parallel plane walls. It was observed that both point contact and line contact with the constraint walls are possible. Roman and Pocheau (1999, 2002) used an elastica model to investigate the response of a buckled thin plate subject to prescribed height reduction. Kuru et al. (2000) studied the buckling behavior of drilling pipes in directional wells. Chen and Li (2007) and Lu and Chen (2008) studied the deformation of a planar elastica inside a circular channel with clearance.

The emphasis of these studies was placed on the static deformations of the constrained elastica. Very often, multiple equilibria under a specified set of loading condition are possible. In order to determine whether a calculated deformation exists in reality, a stability analysis is needed. There is, however, no theory available to determine the stability of these equilibrium configurations. As a consequence, experimental observation has been an important tool to validate the existence of a calculated equilibrium in reality in previous researches. The purpose of this paper is to present a theoretical approach which is capable of predicting the stability of a constrained elastica deformation.

In constrained elastica the lateral constraint is unilateral, i.e., it can exert compression but not tension onto the elastica. Mathematically, this type of constraints can be represented by a set of inequality equations. This poses challenges in determining the critical states of the loaded structure. Frequently, energy method based on the extended principle of total potential is adopted (Villaggio, 1979), assuming that the loaded system is conservative. Klarbring (1988) demonstrated that non-smooth bifurcation points, corner limit points, and end points may exist in unilaterally constrained structures. Schulz and Pellegrino (2000) showed that the equilibrium equations for a multi-body system subject to unilateral constraints have the same form as the standard Kuhn–Tucker conditions in optimization theory. Tschope et al. (2003) used a direct computation technique to solve for the instability points of a contact problem. Rumyantsev (2006) formulated a variational principle for systems with unilateral constraints. Kanno and Ohsaki (2009) proposed to solve a maximization problem of a convex

* Corresponding author. Tel.: +886 2 3366 2693; fax: +886 2 2 2363 1755.
E-mail address: jschen@ntu.edu.tw (J.-S. Chen).

0020-7683/$ - see front matter © 2010 Elsevier Ltd. All rights reserved.
doi:10.1016/j.ijsolstr.2010.04.015

function over a convex set to determine the stability of a given equilibrium point of a unilaterally constrained structure. These papers dealt with the critical states of discrete systems under unilateral constraints.

In the case of continuous systems such as a constrained elastica, Domokos et al. (1997) gave an insightful discussion and concluded that the standard tools, including the energy method, for stability analysis are useless. One of the difficulties of the stability analysis arises from the fact that while the problem is continuous, the relevant functions are non-smooth due to the contact forces. In this paper, we develop a vibration method to calculate the natural frequencies and determine the stability of an elastica constrained by a pair of plane walls. The vibration problem of an elastica without lateral constraint is straightforward and has been well solved; see Santillan et al. (2006) and Chen and Lin (2008). The key of solving the vibration problem in constrained elastica, on the other hand, is to take into account the sliding between the elastica and the space-fixed unilateral constraint during vibration.

In this paper, we first consider the deformation patterns of an elastica constrained inside a pair of symmetrically placed plane walls. We next focus on the formulation of the linearized equations of motion and boundary conditions of the constrained elastica. Natural frequencies and mode shapes of the constrained elastica can then be calculated and the stability of the system may be determined. In order to compare with theoretical predictions, a load-controlled experiment is conducted. The experiment shows that no line-contact deformations exist, a result different from those reported previously by others with different set-ups. Finally, explanations are provided to confirm the validity of these previous investigations and explain the cause of the difference.

2. Problem description

Fig. 1 shows an inextensible elastic strip with the right end fully clamped at point B. The flexural rigidity and the mass density per unit length of the elastic strip are EI and μ, respectively. On the left-hand side there is a straight channel with an opening at point A. The distance between points A and B is L. Part of the strip is allowed to slide without friction and clearance inside the channel. Edge thrust F_A^* is applied at the left end of the strip causing it to buckle in the domain of interest between points A and B. The boundary condition at point A may be called "partially clamped", by which we mean that the strip is allowed to slide freely through the opening A, while the lateral displacement and slope at A are fixed. An x^*y^*-coordinate system is fixed at point A. A set of parallel plane walls at $y^* = \pm h^*$ prevents the elastica from deforming freely. In Fig. 1 the elastica contacts the walls at two points W_1 and W_2 at $s^* = l_1^*$ and l_2^*, where s^* is the length of the elastica measured from point A. The total length l^* of the elastica between A and B varies as the edge thrust increases. It is noted that in most of the previous works on constrained elastica, the total length of the elastica is fixed, except in Chen and Li (2007) and Lu and Chen (2008).

3. Equilibrium configurations

Once the elastica is in contact with the walls, the analysis of the shape of the elastica must be conducted in a piecewise manner. Since the main purpose of this paper is to discuss the dynamic characteristics of the constrained elastica, the detail of the static analysis is omitted here. The interested readers can either follow the shooting method described in Domokos et al. (1997) or the procedure presented in Lu and Chen (2008). In the following, we will discuss the various deformation patterns and the load–deflection relations obtained from static analysis.

For simplicity, the length, force, moment, time, and frequency used in this paper are non-dimensionalized according to the following schemes:

$$(s,l,x,y) = \frac{1}{L}(s^*,l^*,x^*,y^*), \quad F_A = \frac{L^2}{4\pi^2 EI}F_A^*, \quad M = \frac{L}{4\pi^2 EI}M^*$$
$$t = \frac{1}{L^2}\sqrt{\frac{EI}{\mu}}t^*, \quad \omega = L^2\sqrt{\frac{\mu}{EI}}\omega^* \tag{1}$$

All the variables with asterisks on the right-hand sides of these equations are physical variables with dimensions. Their dimensionless counterparts (without asterisks) are on the left-hand sides. Therefore, s, F_A, M, t, and ω are the dimensionless length, force, moment, time, and frequency in the following discussion.

Fig. 2 shows the relation between the edge thrust F_A and the length Δl of the elastica being pushed in through the channel, where $\Delta l = l - 1$. The separation distance $2h$ is set to be 0.2. Deformation loci of different configurations are marked with numbers. The bifurcation points are marked with black dots and lower-case letters. The abrupt terminal point of a locus is marked with a cross symbol, such as points j and q. In the range of Fig. 2, we record 19 different deformation patterns. Holmes et al. (1999) developed a scheme of sheet to categorize the deformations of a constrained elastica. Sheet 0 contains all solutions without contacting the walls. Sheet Pn contains all solutions constrained by the walls at n points. Sheet Ln contains all solutions constrained by the walls in n line segments. According to this scheme, we categorize the deformations in Fig. 2 as follows.

(1) Sheet 0 contains deformations 1, 2, 5, 6, and 8. These are the Euler buckling modes. These loci end when contacts with the walls occur and the deformations transform to other patterns. For instance, locus 5 meets locus 9 at j and terminates there. The phenomenon of locus termination is due to the fact that the walls can provide compressive reaction but not tensile.
(2) Sheet $P1$ contains deformations 3, 4, and 11. Sheet $P2$ contains deformations 9, 10, 12, 13, 16, and 19. Sheet $P3$ contains deformations 14, 17, and 18.
(3) Sheet $L1$ contains deformations 7. Sheet $L2$ contains deformations 15.

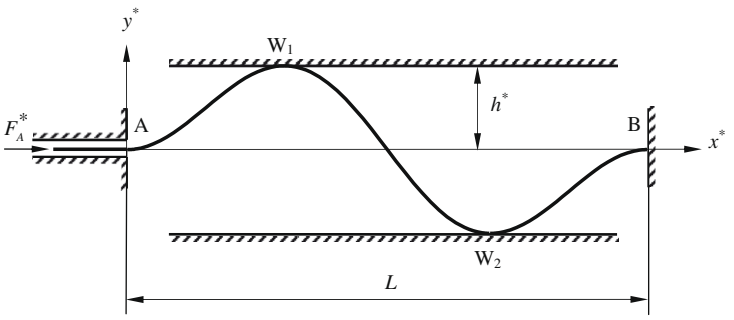

Fig. 1. An elastica constrained by a pair of plane walls. The elastica is fixed at point B and fed into the domain of interest AB from opening A under edge thrust F_A^*.

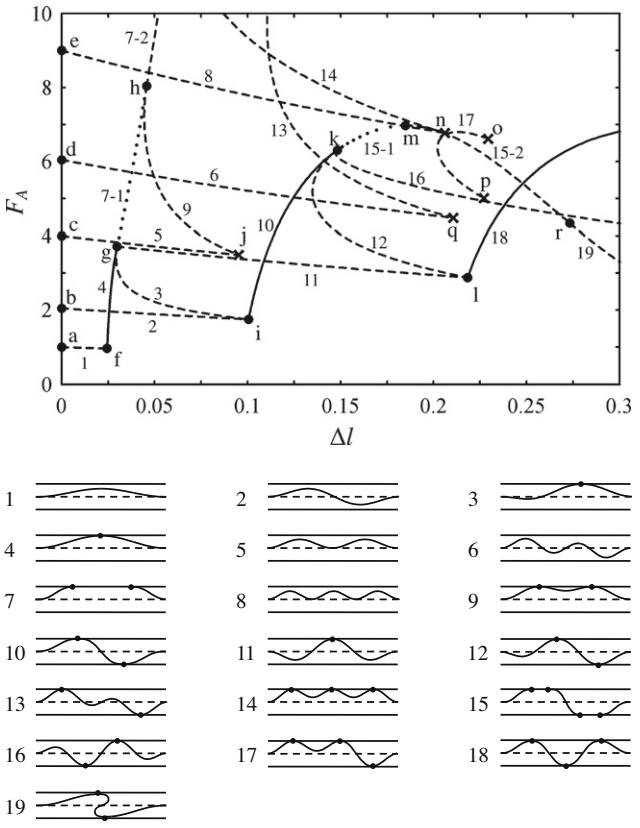

Fig. 2. Load–deflection curves for a constrained elastica under load control with $h = 0.1$. The solid, dashed, and dotted lines represent stable, unstable and neutral solutions, respectively.

Static analysis allows us to find all the possible equilibrium configurations as shown in Fig. 2. However, not all these equilibrium configurations are stable. In this paper, we develop a dynamic method to calculate the natural frequencies of each equilibrium state. If all the natural frequencies are real and greater than zero, the equilibrium configuration is stable and the associated locus is traced with solid line. If any one of the natural frequencies is imaginary, the equilibrium state is unstable and the associated locus is traced with dashed line. If all the natural frequencies are real but at least one of them is zero, the stability of the equilibrium state cannot be determined from the linear vibration analysis. We refer this type of solution as neutral, and the associated locus is traced with dotted line. The stability properties of the constrained elastica are dependent upon the loading mechanism at point A. The stability properties presented in Fig. 2 are for a constrained elastica under load control.

It is noted that the slopes of all the loci in sheet 0 are negative. The corresponding deformations are all unstable. Take locus 1 as an example. The elastic strip buckles at point a via a sub-critical bifurcation. We expect that the elastic strip jumps from point a to a point slightly above point f on locus 4 as the edge thrust increases quasi-statically. It is noted that this type of sub-critical bifurcation is due to the variable-length feature of the elastica, see Wang et al. (1998) and Chen and Ro (2010). A column with fixed length (Domokos et al., 1997; Chai, 1998) will buckle via a super-critical bifurcation with the nontrivial equilibrium path rising as the load increases. There will be no jump in the fixed-length problem.

Locus 7 (one-line contact) is composed of two parts; one with dotted line (7-1 between g and h) and the other with dashed line (7-2 beyond h). The length of line contact increases from point g all the way to beyond h. At the bifurcation point h, the length of the contact segment and the axial force happen to satisfy the condition of Euler buckling. Another branch 9 of two-point contact emerges from point h and terminates at j. The bifurcation at point h is called secondary buckling by some researchers. It is tempting to assume that the line-contact deformation is stable until the secondary buckling occurs. Although this is true for a pinned–pinned elastica as discussed in Domokos et al. (1997), it is not necessarily true for the clamped–clamped case. For the constrained elastica discussed in this paper, buckling occurs earlier at point g instead of point h. It is noted that Chai (1998) and Roman and Pocheau (1999) conducted experiments on clamped–clamped elastica and did observe line-contact deformations, which became unstable via secondary buckling. However, in these experiments the plane walls are on $y = 0$ and h, instead of $y = \pm h$. The reason why the elastica under different plane wall set-up behaves so differently will be discussed in more detail in Section 7.

Locus 15 (two-line contact) is the extension of locus 10 (two-point contact) and is composed of 15-1 (dotted, between k and m) and 15-2 (dashed, between m and r). Point m is a limit point (with a horizontal tangent) of locus 15. The length of contact segment increases from point k to a maximum and then decreases all the way to point r. Beyond point r, the deformation evolves to another two-point contact configuration 19. Another interesting phenomenon worth mentioning is that each point on loci 15-1 and 15-2 actually represents an infinite number of similar deformations. The contact lengths on the upper and the lower walls are not necessarily equal. All similar deformations with different contact length combination would satisfy the same equilibrium equations as long as the sum of the two contact lengths remains unchanged. Similar feature was reported by Roman and Pocheau (1999) in a different set-up. It is noted that this feature does not exist for the one-line contact deformations 7-1 and 7-2.

For the load-control problem in Fig. 2, some rules may be summarized as follows. For those loci with negative slopes the deformations are always unstable. This is equivalent to a spring with negative stiffness or a gas with negative compressibility. On the other hand, a positive slope does not necessarily mean a stable equilibrium. These simple rules may help discriminate quickly some of the unstable branches. However, these rules do not apply to displacement-control procedure as described in Section 5.

4. Vibration and stability analysis

As mentioned above, the deformation patterns discussed in Section 3 may not be stable. If the deformation is unstable, then it will not exist in reality. It is noted that the elastica may be in point or in line contact with the walls, sometimes at multiple locations. In this paper, we assume that all the contacts are frictionless. In the following, we introduce a vibration method which is capable of determining the natural frequencies and mode shapes of the constrained elastica.

4.1. Two-point contact on different walls

We first consider the case when the equilibrium configuration involves two-point contact on different walls, such as the one corresponding to locus 10 in Fig. 2. The deformation pattern is also shown in Fig. 1. The two contact points W_1 and W_2 are at $s = l_1$ and l_2, respectively. This analysis can be readily extended to other contact situations.

4.1.1. Lagrangian and Eulerian descriptions

For a small element ds near the contact point W_1 we can write the geometrical relations, balance of moment and forces, and moment–curvature relation, in their dimensionless forms, as

$$\frac{\partial x(s,t)}{\partial s} = \cos\theta(s,t) \tag{2}$$

$$\frac{\partial y(s,t)}{\partial s} = \sin\theta(s,t) \tag{3}$$

$$\frac{\partial M(s,t)}{\partial s} = F_x(s,t)\sin\theta(s,t) - F_y(s,t)\cos\theta(s,t) \tag{4}$$

$$\frac{\partial F_x(s,t)}{\partial s} = \frac{1}{4\pi^2}\frac{\partial^2 x(s,t)}{\partial t^2} \tag{5}$$

$$\frac{\partial F_y(s,t)}{\partial s} - R_{y1}(t)\delta(s - l_1 - \eta_1(t)) = \frac{1}{4\pi^2}\frac{\partial^2 y(s,t)}{\partial t^2} \tag{6}$$

$$\frac{\partial \theta(s,t)}{\partial s} = 4\pi^2 M(s,t) \tag{7}$$

$F_x(s,t)$ and $F_y(s,t)$ are the internal forces in the x and y directions. θ is the rotation angle of the strip. $R_{y1}(t)$ is the normal force exerted by the wall on the elastica at the contact point. $\delta(\cdot)$ is the dimensionless Dirac delta function. Eq. (6) is valid for the elastica between points A and W_2, i.e., for $0 < s < l_2$. These six equations can be called the Lagrangian version of the governing equations. s may be called the Lagrangian coordinate of a point on the elastica.

It is noted that $s = l_1$ represents the material point of the contact point W_1 when the elastica is in equilibrium. During vibration, the elastica may slide on the wall. As a consequence, the contact point on the elastica may change from $s = l_1$ to $s = l_1 + \eta_1$, where $\eta_1(t)$ is a small number. This change of contact point is reflected in Eq. (6).

We denote the static solutions of Eqs. (2)–(7) $x_e(s)$, $y_e(s)$, $\theta_e(s)$, $M_e(s)$, $F_{xe}(s)$, $F_{ye}(s)$, and constant R_{y1e}. $F_{ye}(s)$ can be written as

$$F_{ye}(s) = F_{ye}(s)\big|_{s=0} + R_{y1e}H(s - l_1) \tag{8}$$

H is the Heaviside step function. During vibration, the function $F_y(s,t)$ may be regarded as the superposition of $F_{ye}(s)$ and a small harmonic perturbation, expressed mathematically as

$$F_y(s,t) = F_{ye}(s) + \left[R_{y1e}(H(s - l_1 - \eta_1) - H(s - l_1))\right] + \left[\widehat{F}_{yd}(s - \eta_1) + R_{y1d}H(s - l_1 - \eta_1)\right]\sin\omega t \tag{9}$$

ω is a natural frequency of the constrained elastica. A variable with subscript "d" represents a small perturbation of its static counterpart with subscript "e". The first bracket on the right-hand side of Eq. (9) represents the shift of the contact point from $s = l_1$ to $s = l_1 + \eta_1$. After using Eq. (8), Eq. (9) can be rewritten as

$$F_y(s,t) = F_{ye}(s - \eta_1) + \left[\widehat{F}_{yd}(s - \eta_1) + R_{y1d}H(s - l_1 - \eta_1)\right]\sin\omega t \tag{10}$$

After defining a new variable ε_1 as

$$\varepsilon_1 = s - \eta_1 \tag{11}$$

Eq. (10) can be rewritten as

$$\widehat{F}_y(\varepsilon_1,t) = F_{ye}(\varepsilon_1) + \left[\widehat{F}_{yd}(\varepsilon_1) + R_{y1d}H(\varepsilon_1 - l_1)\right]\sin\omega t \tag{12}$$

where $\widehat{F}_y(\varepsilon_1,t) = F_y(\varepsilon_1 + \eta_1, t)$. $\widehat{F}_y$ and F_y are two different functions. It is noted that $F_{ye}(\varepsilon_1)$ is the static solution as obtained from static analysis, except that the independent variable s is replaced by ε_1. Similarly, the other perturbed functions may be written as

$$\widehat{F}_x(\varepsilon_1,t) = F_{xe}(\varepsilon_1) + \widehat{F}_{xd}(\varepsilon_1)\sin\omega t \tag{13}$$

$$\hat{x}(\varepsilon_1,t) = x_e(\varepsilon_1) + \hat{x}_d(\varepsilon_1)\sin\omega t \tag{14}$$

$$\hat{y}(\varepsilon_1,t) = y_e(\varepsilon_1) + \hat{y}_d(\varepsilon_1)\sin\omega t \tag{15}$$

$$\hat{\theta}(\varepsilon_1,t) = \theta_e(\varepsilon_1) + \hat{\theta}_d(\varepsilon_1)\sin\omega t \tag{16}$$

$$\widehat{M}(\varepsilon_1,t) = M_e(\varepsilon_1) + \widehat{M}_d(\varepsilon_1)\sin\omega t \tag{17}$$

ε_1 defined in Eq. (11) may be called the Eulerian coordinate of a point of the elastica. $\varepsilon_1 = l_1$ represents the point of the elastica grazing through the wall at W_1 during vibration. It can be different material point at different instant.

By noting that $\frac{\partial \varepsilon_1}{\partial s} = 1$, the Lagrangian version of the governing equations (2)–(7) can now be transformed into the Eulerian version as

$$\frac{\partial \hat{x}(\varepsilon_1,t)}{\partial \varepsilon_1} = \cos\hat{\theta}(\varepsilon_1,t) \tag{18}$$

$$\frac{\partial \hat{y}(\varepsilon_1,t)}{\partial \varepsilon_1} = \sin\hat{\theta}(\varepsilon_1,t) \tag{19}$$

$$\frac{\partial \widehat{M}(\varepsilon_1,t)}{\partial \varepsilon_1} = \widehat{F}_x(\varepsilon_1,t)\sin\hat{\theta}(\varepsilon_1,t) - \widehat{F}_y(\varepsilon_1,t)\cos\hat{\theta}(\varepsilon_1,t) \tag{20}$$

$$\frac{\partial \widehat{F}_x(\varepsilon_1,t)}{\partial \varepsilon_1} = \frac{1}{4\pi^2}\frac{\partial^2 \hat{x}(\varepsilon_1,t)}{\partial t^2} \tag{21}$$

$$\frac{\partial \widehat{F}_y(\varepsilon_1,t)}{\partial \varepsilon_1} - R_{y1}(t)\delta(\varepsilon_1 - l_1) = \frac{1}{4\pi^2}\frac{\partial^2 \hat{y}(\varepsilon_1,t)}{\partial t^2} \tag{22}$$

$$\frac{\partial \hat{\theta}(\varepsilon_1,t)}{\partial \varepsilon_1} = 4\pi^2\widehat{M}(\varepsilon_1,t) \tag{23}$$

By substituting Eqs. (12)–(17), together with the relations

$$R_{y1}(t) = R_{y1e} + R_{y1d}\sin\omega t \tag{24}$$

$$\eta_1(t) = \eta_{1d}\sin\omega t \tag{25}$$

into Eqs. (18)–(23) and ignoring the higher-order terms, we arrive at the following linear equations for the six functions $\hat{x}_d(\varepsilon_1)$, $\hat{y}_d(\varepsilon_1)$, $\hat{\theta}_d(\varepsilon_1)$, $\widehat{M}_d(\varepsilon_1)$, $\widehat{F}_{xd}(\varepsilon_1)$, and $\widehat{F}_{yd}(\varepsilon_1)$:

$$\frac{d\hat{x}_d(\varepsilon_1)}{d\varepsilon_1} = -\hat{\theta}_d(\varepsilon_1)\sin\theta_e(\varepsilon_1) \tag{26}$$

$$\frac{d\hat{y}_d(\varepsilon_1)}{d\varepsilon_1} = \hat{\theta}_d(\varepsilon_1)\cos\theta_e(\varepsilon_1) \tag{27}$$

$$\frac{d\hat{\theta}_d(\varepsilon_1)}{d\varepsilon_1} = 4\pi^2\widehat{M}_d(\varepsilon_1) \tag{28}$$

$$\frac{d\widehat{M}_d(\varepsilon_1)}{d\varepsilon_1} = \left[F_{xe}(\varepsilon_1)\hat{\theta}_d(\varepsilon_1) - \widehat{F}_{yd}(\varepsilon_1) - R_{y1d}H(\varepsilon_1 - l_1)\right]\cos\theta_e + \left[F_{ye}(\varepsilon_1)\hat{\theta}_d(\varepsilon_1) + \widehat{F}_{xd}(\varepsilon_1)\right]\sin\theta_e \tag{29}$$

$$\frac{d\widehat{F}_{xd}(\varepsilon_1)}{d\varepsilon_1} = \frac{1}{4\pi^2}\omega^2[\cos\theta_e(\varepsilon_1)\eta_{1d} - \hat{x}_d(\varepsilon_1)] \tag{30}$$

$$\frac{d\widehat{F}_{yd}(\varepsilon_1)}{d\varepsilon_1} = \frac{1}{4\pi^2}\omega^2[\sin\theta_e(\varepsilon_1)\eta_{1d} - \hat{y}_d(\varepsilon_1)] \tag{31}$$

Eqs. (26)–(31) are valid in the range $0 < \varepsilon_1 < l_2$.

The above formulation can be repeated for the elastica between points W_1 and B by replacing all the subscript "1" by "2", and a single over-hat (such as $\hat{x}_d$) by a double over-hat $\left(\hat{\hat{x}}_d\right)$. As a consequence we have another set of equations similar to Eqs. (26)–(31) after introducing another Eulerian coordinate ε_2 as

$$\varepsilon_2 = s - \eta_2 \tag{32}$$

where $l_1 < \varepsilon_2 < l.\eta_2$ represents the sliding movement at contact point W_2. The functions $\hat{x}_d(\varepsilon_1)$, $\hat{y}_d(\varepsilon_1)$, $\hat{\theta}_d(\varepsilon_1)$, $\widehat{M}_d(\varepsilon_1)$, $\widehat{F}_{xd}(\varepsilon_1)$, and $\widehat{F}_{yd}(\varepsilon_1)$ in Eqs. (26)–(31) are replaced by a different set of functions $\hat{\hat{x}}_d(\varepsilon_2)$, $\hat{\hat{y}}_d(\varepsilon_2)$, $\hat{\hat{\theta}}_d(\varepsilon_2)$, $\widehat{\widehat{M}}_d(\varepsilon_2)$, $\widehat{\widehat{F}}_{xd}(\varepsilon_2)$, and $\widehat{\widehat{F}}_{yd}(\varepsilon_2)$.

4.1.2. Boundary conditions

In load control, the elastica is allowed to retreat into and protrude out of the opening A during vibration. This small length of movement is denoted $\eta_0(t)$ and can be expressed as

$$\eta_0(t) = \eta_{0d}\sin\omega t \tag{33}$$

The exact geometrical boundary conditions at opening A require that

$$\theta(s,t)|_{s=\eta_0} = \hat{\theta}(\varepsilon_1,t)\Big|_{\varepsilon_1=\eta_0-\eta_1} = 0 \tag{34}$$

$$x(s,t)|_{s=\eta_0} = \hat{x}(\varepsilon_1,t)|_{\varepsilon_1=\eta_0-\eta_1} = 0 \tag{35}$$

$$y(s,t)|_{s=\eta_0} = \hat{y}(\varepsilon_1,t)|_{\varepsilon_1=\eta_0-\eta_1} = 0 \tag{36}$$

These geometrical boundary conditions can be linearized to the forms

$$\hat{\theta}_d(\varepsilon_1)\Big|_{\varepsilon_1=0} = 4\pi^2 M_e(\varepsilon_1)|_{\varepsilon_1=0}(\eta_{1d}-\eta_{0d}) \tag{37}$$

$$\hat{x}_d(\varepsilon_1)|_{\varepsilon_1=0} = \eta_{1d}-\eta_{0d} \tag{38}$$

$$\hat{y}_d(\varepsilon_1)|_{\varepsilon_1=0} = 0 \tag{39}$$

The dynamic boundary condition F_A = constant yields

$$\widehat{F}_{xd}(\varepsilon_1)\Big|_{\varepsilon_1=0} = 0 \tag{40}$$

Similarly, the boundary conditions at the fixed end B can be linearized to the forms

$$\hat{\hat{\theta}}_d(\varepsilon_2)\Big|_{\varepsilon_2=l} = 4\pi^2 M_e(\varepsilon_2)|_{\varepsilon_2=l}\eta_{2d} \tag{41}$$

$$\hat{\hat{x}}_d(\varepsilon_2)\Big|_{\varepsilon_2=l} = \eta_{2d} \tag{42}$$

$$\hat{\hat{y}}_d(\varepsilon_2)\Big|_{\varepsilon_2=l} = 0 \tag{43}$$

4.1.3. Contact conditions

During vibration, the elastica is always in contact with and is allowed to slide on the wall without friction. The exact contact condition at W_1 can be written as

$$\theta(s,t)|_{s=l_1+\eta_1} = \hat{\theta}(\varepsilon_1)\Big|_{\varepsilon_1=l_1} = 0 \tag{44}$$

$$y(s,t)|_{s=l_1+\eta_1} = \hat{y}(\varepsilon_1)|_{\varepsilon_1=l_1} = h \tag{45}$$

These two conditions at W_1 can be rewritten as (without linearization)

$$\hat{\theta}_d(\varepsilon_1)\Big|_{\varepsilon_1=l_1} = 0 \tag{46}$$

$$\hat{y}_d(\varepsilon_1)|_{\varepsilon_1=l_1} = 0 \tag{47}$$

Similarly, the contact conditions at W_2 are

$$\hat{\hat{\theta}}_d(\varepsilon_2)\Big|_{\varepsilon_2=l_2} = 0 \tag{48}$$

$$\hat{\hat{y}}_d(\varepsilon_2)\Big|_{\varepsilon_2=l_2} = 0 \tag{49}$$

4.1.4. Transition from ε_1 to ε_2

It is noted that we have defined two Eulerian coordinates ε_1 and ε_2. The location of a material point on the elastica can be expressed in terms of either ε_1 or ε_2. For instance, the contact point W_2 can be defined either as $\varepsilon_2 = l_2$ or $\varepsilon_1 = l_2 + \eta_2 - \eta_1$. As a consequence, a function can be written in terms of either ε_1 or ε_2. For example, the rotation angle at W_2 can be written as

$$\theta(s,t)|_{s=l_2+\eta_2} = \hat{\hat{\theta}}(\varepsilon_2,t)\Big|_{\varepsilon_2=l_2} = \hat{\theta}(\varepsilon_1,t)\Big|_{\varepsilon_1=l_2+\eta_2-\eta_1} \tag{50}$$

After superposing a small harmonic perturbation on the static equilibrium, Eq. (50) can be written as

$$\theta_e(\varepsilon_2)|_{\varepsilon_2=l_2} + \hat{\hat{\theta}}_d(\varepsilon_2)\Big|_{\varepsilon_2=l_2}\sin\omega t = \theta_e(\varepsilon_1)|_{\varepsilon_1=l_2+\eta_2-\eta_1} + \hat{\theta}_d(\varepsilon_1)\Big|_{\varepsilon_1=l_2+\eta_2-\eta_1}\sin\omega t \tag{51}$$

After expanding the two functions $\theta_e(\varepsilon_1)$ and $\hat{\theta}_d(\varepsilon_1)$ on the right-hand side with respect to $\varepsilon_1 = l_2$, Eq. (51) can be linearized to the form

$$\hat{\hat{\theta}}_d(\varepsilon_2)\Big|_{\varepsilon_2=l_2} = \hat{\theta}_d(\varepsilon_1)\Big|_{\varepsilon_1=l_2} + \frac{\partial\theta_e}{\partial\varepsilon_1}\Big|_{\varepsilon_1=l_2}(\eta_{2d}-\eta_{1d}) \tag{52}$$

Similar equations for $\hat{x}_d$, $\hat{y}_d$, $\widehat{\widehat{M}}_d$, $\hat{\widehat{F}}_{xd}$, and $\hat{\widehat{F}}_{yd}$ can be obtained in the same manner.

4.1.5. Solution method

In summary, we have two sets of six linearized differential equations, like the ones in (26)–(31). These differential equations, together with the boundary conditions and contact conditions, admit nontrivial solutions only when ω is equal to the eigenvalue of the system of equations. The unknowns to be found are: the two sets of six functions $\hat{x}_d$, $\hat{y}_d$, $\hat{\theta}_d$, $\widehat{M}_d$, $\widehat{F}_{xd}$, $\widehat{F}_{yd}$, and $\hat{\hat{x}}_d$, $\hat{\hat{y}}_d$, $\hat{\hat{\theta}}_d$, $\widehat{\widehat{M}}_d$, $\hat{\widehat{F}}_{xd}$, $\hat{\widehat{F}}_{yd}$, the amplitudes of sliding η_{0d}, η_{1d}, η_{2d}, the dynamic shear force $\widehat{F}_{yd}(\varepsilon_1)\Big|_{\varepsilon_1=0}$ and bending moment $\widehat{M}_d(\varepsilon_1)\Big|_{\varepsilon_1=0}$ at point A, and the two dynamic normal reactions R_{y1d} and R_{y2d} at the contact points. It is noted that ω in Eqs. (30) and (31) only appears in the form of ω^2. Therefore, if the characteristic value ω^2 is positive, the corresponding mode is stable with natural frequency ω. On the other hand, the equilibrium configuration is unstable if ω^2 is negative.

A shooting method is used to solve for the characteristic value ω^2. We first set $\widehat{M}_d(\varepsilon_1)\Big|_{\varepsilon_1=0} = 1$. After guessing seven variables $\widehat{F}_{yd}(\varepsilon_1)\Big|_{\varepsilon_1=0}$, R_{yd1}, R_{yd2}, η_{0d}, η_{1d}, η_{2d}, and ω^2, we can integrate Eqs. (26)–(31) like an initial value problem all the way from $\varepsilon_1 = 0$ to $\varepsilon_1 = l_2$. The four boundary conditions (37)–(40) at point A provide the needed initial conditions. At $\varepsilon_1 = l_2$ the six values of $\hat{x}_d(\varepsilon_1)|_{\varepsilon_1=l_2}$, $\hat{y}_d(\varepsilon_1)|_{\varepsilon_1=l_2}$, $\hat{\theta}_d(\varepsilon_1)\Big|_{\varepsilon_1=l_2}$, $\widehat{M}_d(\varepsilon_1)\Big|_{\varepsilon_1=l_2}$, $\widehat{F}_{xd}(\varepsilon_1)\Big|_{\varepsilon_1=l_2}$, and $\widehat{F}_{yd}(\varepsilon_1)\Big|_{\varepsilon_1=l_2}$ can be used to calculate $\hat{\hat{x}}_d(\varepsilon_2)\Big|_{\varepsilon_2=l_2}$, $\hat{\hat{y}}_d(\varepsilon_2)\Big|_{\varepsilon_2=l_2}$, $\hat{\hat{\theta}}_d(\varepsilon_2)\Big|_{\varepsilon_2=l_2}$, $\widehat{\widehat{M}}_d(\varepsilon_2)\Big|_{\varepsilon_2=l_2}$, $\hat{\widehat{F}}_{xd}(\varepsilon_2)\Big|_{\varepsilon_2=l_2}$, and $\hat{\widehat{F}}_{yd}(\varepsilon_2)\Big|_{\varepsilon_2=l_2}$ according to the transition equations similar to Eq. (52). From here on ε_2 becomes the independent variable and the integration continues until $\varepsilon_2 = l$. The three boundary conditions (41)–(43) at $\varepsilon_2 = l$, two contact equations (46) and (47) at $\varepsilon_1 = l_1$, and two contact conditions (48) and (49) at $\varepsilon_2 = l_2$ are used to check the accuracy of the seven guesses. If the guesses are not satisfactory, a new set of guesses is adopted.

4.2. Other contact situations

The above analysis can be readily extended to other point-contact cases. For instance, for one-point contact, only one Eulerian coordinate ε_1 is needed. For three-point contact, three Eulerian coordinates ε_1, ε_2, and ε_3 are needed.

The vibration analysis of one-line contact is similar to the one in the two-point contact situation discussed in Section 4.1. In the analysis, the two ends of the contact segment are treated as the two points W_1 and W_2 in Section 4.1. The main difference is that in the line-contact case the calculated mode shape must be checked whether it violates the wall constraint. If a mode shape penetrates the wall during vibration, the mode is invalid and must be discarded. The analysis of two-line contact is similar, although more complicated. Four Eulerian coordinates ε_1, ε_2, ε_3, and ε_4 must be defined in the case of two-line contact.

4.3. Numerical results and discussions

4.3.1. Transition from one-point to one-line contact

Fig. 3 shows the ω^2 as functions of the edge thrust F_A (starting from 0.964) for deformations along loci 4, 7-1, and 7-2 (passing

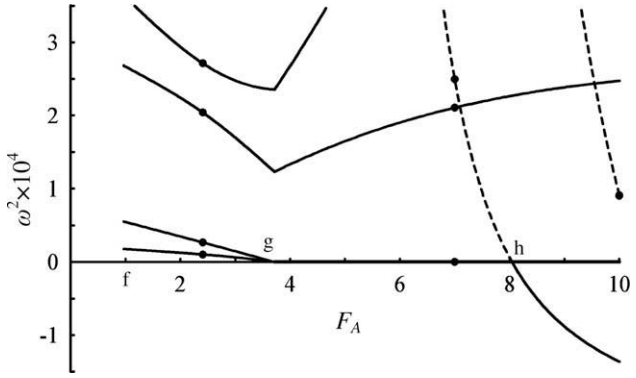

Fig. 3. ω^2 as functions of the edge thrust F_A for deformations along loci 4, 7-1, and 7-2 in Fig. 2. Dashed lines represent invalid modes which will penetrate the wall during vibration. The mode shapes of those modes marked with black dots are shown in Figs. 4–6.

points f, g, and h) in Fig. 2. It is noted that all ω^2 decrease as F_A increases from point f to g. The first two ω^2 approach zero together as F_A approaches point g. Because all the ω^2 between points f and g are positive, we conclude that the one-point contact deformation 4 is stable. Fig. 4 shows the first four mode shapes when $(F_A, \Delta l) = (2.404, 0.0262)$. The square of the natural frequencies ω^2 are 1023.66, 2689.66, 20427.6, and 27160.0, respectively. The solid and dashed lines in Fig. 4 represent the equilibrium configurations and the vibrating mode shapes, respectively. The same format applies to all the mode shapes presented in this paper. These mode shapes are not strictly symmetric or anti-symmetric because the two ends A and B are not exactly identical. However, we can still observe that the first and the second modes are roughly anti-symmetric and symmetric, respectively. The sliding of the elastica on the constraint wall during vibration is obvious in the first mode.

The lowest two ω^2 merge at point g and remain zero from this point on through point h and beyond. In the range between points g and h, which corresponds to deformation 7-1, the lowest two ω^2 are zero. Therefore, we have no conclusion regarding the stability of the deformation in this range. Fig. 5 shows the first four mode shapes when $(F_A, \Delta l) = (7, 0.0422)$. The corresponding ω^2 are 0, 0, 21053.3, and 24988.8, respectively. In the first mode shape the only non-zero eigenfunctions are $\hat{x}_d(\varepsilon_1)$ and η_{1d}. On the other hand, $\hat{\hat{x}}_d(\varepsilon_2)$ and η_{2d} are the only non-zero eigenfunctions in the second mode. It is noted that the zero natural frequencies and the corresponding mode shapes described above can be analytically proved to satisfy Eqs. (26)–(31) and the associated boundary conditions. Therefore, the lowest two natural frequencies are "exactly" zero but not just small numerically. The fourth mode shows that the line-contact part will leave the wall during half of the period of the vibration. This mode is invalid because it will penetrate the wall during the other half of the period. The ω^2-curve corresponding to this mode is traced with dashed line. We keep the dashed curve in the figure solely to demonstrate that invalid mode may appear from our analysis.

For the range beyond point h, there is always one mode whose ω^2 is negative. For instance, there are five modes in the range of Fig. 4 when $(F_A, \Delta l) = (10, 0.0520)$, whose ω^2 are -13644.3, 0, 0, 9078.91, and 24735.84, respectively. The mode corresponding to the negative ω^2 is similar to the fourth mode in Fig. 5. While this mode shape is an invalid vibration mode in the range between points g and h, it is a valid buckling mode because it complies with the wall constraint as the elastica buckles away from the wall and never comes back. Therefore, we trace this negative ω^2 locus with solid line. The second and the third modes have zero ω^2 and the corresponding mode shapes are similar to the ones in Fig. 5(a) and (b). The fourth mode at $\omega^2 = 9078.91$ is shown in Fig. 6. This mode is invalid because it does not comply with the wall constraint at any time.

4.3.2. Transition from two-point to two-line contact

We now examine the dynamic characteristics of the equilibrium configurations on loci 10, 15-1, 15-2, and 19 (passing points

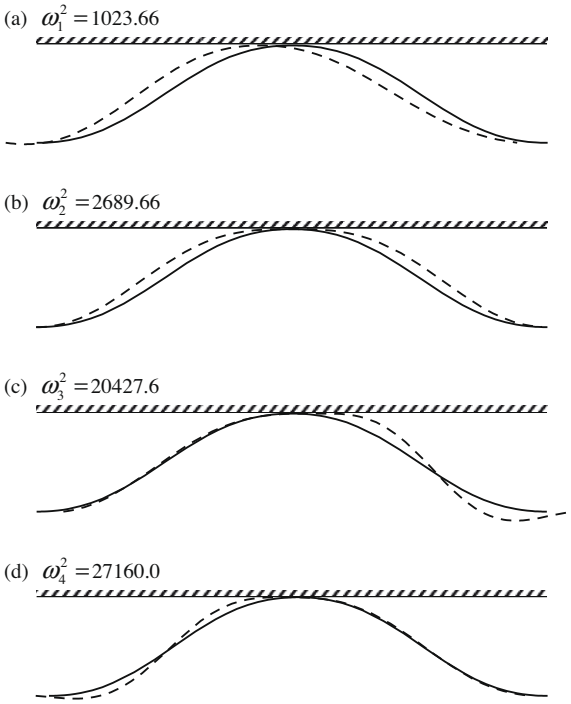

Fig. 4. The first four mode shapes of the one-point contact deformation on locus 4 when $(F_A, \Delta l) = (2.404, 0.0262)$. The solid and the dashed lines represent equilibrium configurations and vibrating mode shapes, respectively.

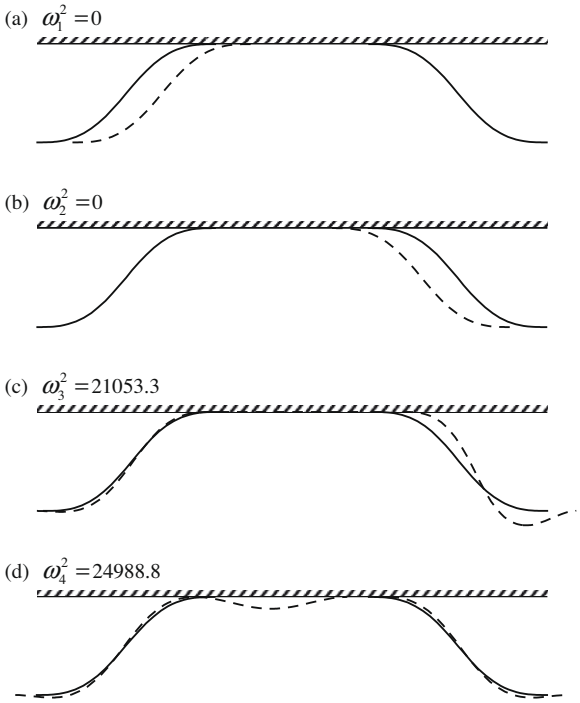

Fig. 5. The first four mode shapes of the one-line contact deformation on locus 7-1 when $(F_A, \Delta l) = (7, 0.0422)$. The fourth mode (d) is invalid because it violates the wall constraint during half of the period of vibration.

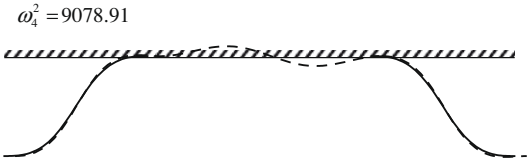

Fig. 6. The fourth mode shape of the one-line contact deformation on locus 7-2 when $(F_A, \Delta l) = (10, 0.0520)$. This is an invalid mode.

i, k, m, and r). Fig. 7 shows the first four ω^2 as functions of the length increment Δl starting from 0.1005 (point i). We choose Δl as an independent parameter in Fig. 7 instead of F_A because ω^2 is a single-valued function of Δl in this range, but not F_A. In the range from point i to k, all the ω^2 are positive. Therefore, all the two-point contact deformations corresponding to locus 10 in Fig. 2 are stable. It is noted that the first three ω^2 approach zero together at point k, and remain zero until point r.

In the range between points k and m, the lowest three ω^2 are zero. As a consequence, the stability is inconclusive for locus 15-1. In the range between points m and r, the lowest ω^2 is negative. Therefore, the two-line contact deformation corresponding to locus 15-2 is unstable. Fig. 8 shows the first four mode shapes when $(F_A, \Delta l) = (6.865, 0.2)$. The three mode shapes corresponding to the degenerate natural frequencies of zero are shown in Fig. 8(b)–(d). In each of these modes, only one of the three non-contact segments moves during vibration.

As Δl increases beyond point r, the deformation evolves back to two-point contact (locus 19) and the three degenerate natural frequencies of zero break up. The first four ω^2 when $(F_A, \Delta l) = (2.300, 0.3)$ are -2359.74, 36.93, 1910.64, and 1958.08. Since the lowest ω^2 is negative, this two-point contact deformation is unstable.

5. Some remarks on displacement control

In the case when the elastica is under displacement control, the analysis requires some modifications, and the stability of the constrained elastica may be changed. In this section, we describe the results briefly.

The main difference between the displacement-control and load-control procedures is the boundary conditions at point A. For displacement control, the sliding movement at opening A during vibration is not allowed. As a result, the sliding parameter η_0 does not exist. The three geometric boundary conditions (37)–(39) for load control are modified by removing η_0 from these equations. Furthermore, the boundary condition on the edge thrust, Eq. (40), is no longer needed.

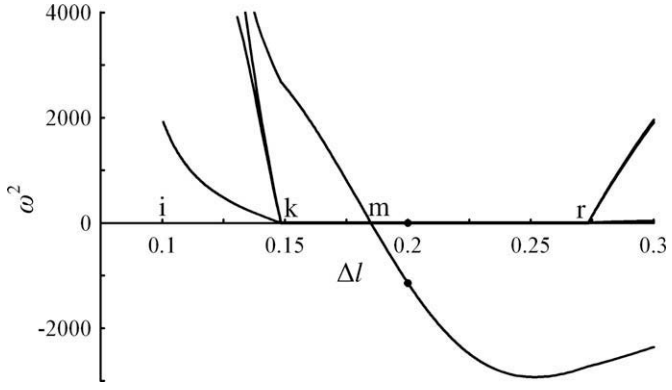

Fig. 7. ω^2 as functions of length increment Δl for deformations along loci 10, 15-1, 15-2, and 19. The mode shapes of those modes marked with black dots are shown in Fig. 8.

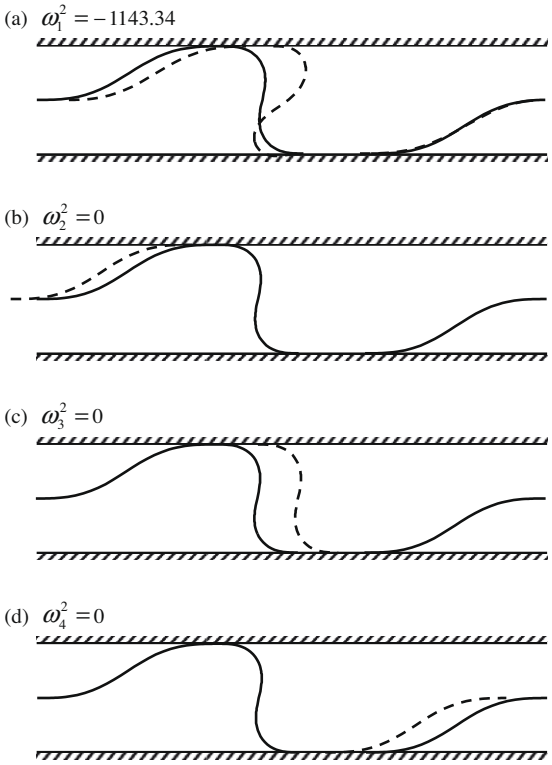

Fig. 8. The first four mode shapes of the two-line contact deformation on locus 15-2 when $(F_A, \Delta l) = (6.865, 0.2)$. The solid and the dashed lines represent equilibrium configurations and vibrating mode shapes, respectively.

Fig. 9 shows the stability of the constrained elastica under displacement control for $h = 0.1$. By comparing with its load-control counterpart in Fig. 2, we can observe some differences in stability between the two procedures. (1) The deformations 3, 9, 12, and 17 are unstable in load control. However, in displacement control part of each of these loci is unstable and the other part is stable, separated by a limit point (with a vertical tangent). The limit points on loci 3 and 9 are very close to the bifurcation points g and h, respectively. Therefore, they are not obvious. However, the limit points on loci 12 and 17 are obvious. Take locus 12 as an example. The limit point is at $(F_A, \Delta l) = (5.189, 0.1349)$. The upper branch above this limit point is unstable, while the lower branch is stable. (2) While the non-contact deformation 1 is unstable in load control,

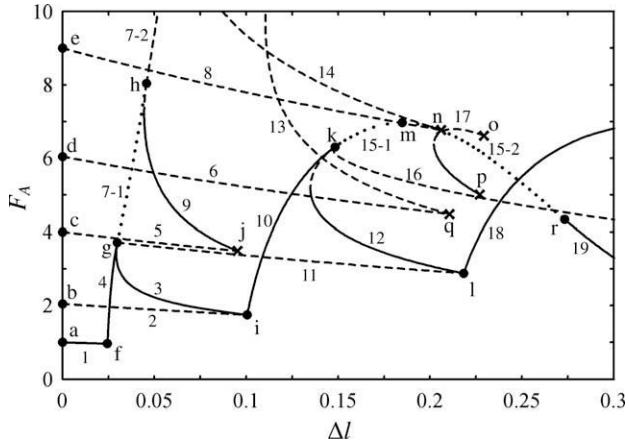

Fig. 9. Load–deflection curves for a constrained elastica under displacement control with $h = 0.1$. The solid, dashed, and dotted lines represent stable, unstable and neutral solutions, respectively.

it is stable in displacement control. (3) While the two-point contact deformation 19 with the reversed "S" shape in the middle is unstable under load control, it is stable in displacement control. (4) While the lowest ω^2 is negative in deformation 15-2 under load control, the three lowest ω^2 remain zero in displacement control. Therefore, the dashed curve of locus 15-2 in Fig. 2 is replaced by a dotted line. In spite of these differences, one important result is not changed by displacement control, i.e., the natural frequencies of deformations 7-1 and 15-1 remain degenerately zero, like the case in load control.

6. Load-control experiment

The foregoing vibration analysis indicates that the stability of line-contact deformations 7-1 and 15-1 is inconclusive, both in load and displacement controls. In order to observe what would happen in reality we designed an experimental set-up for load control, whose top view is shown in Fig. 10. The elastica is made of carbon steel (type SK5) with Young's modulus 205 GPa and mass density 7830 kg/m^3. The cross section of the elastica is 46 mm $\times$ 0.1 mm. The right end of the strip is fully clamped in an aluminum block, which corresponds to point B in Fig. 1. To simulate the partial clamp on the left end of the domain of interest we installed two pairs of rollers in another aluminum block. This design ensures that the strip in the partial clamp remains straight before it is fed through point A. The rollers are to minimize the friction between the strip and the feeding channel. The distance between points A and B is 30 cm. The left end of the strip is fully clamped in a slider, which is allowed to slide along a set of guiding rods. Two strings are attached to this slider, one on the top and the other on the bottom. The strings pass through two pulleys, with the other end attached to a hanging bag. Steel screws, each weighs 11.4 g, are added to the bag to simulate the thrust on the left end of the strip. The wall constraint is made of a pair of aluminum plates. The distance between the two plane walls is 6 cm.

The measured relations between F_A and Δl are plotted with black dots • (loading) and cross marks $\times$ (unloading) in Fig. 11. The solid curves (stable equilibrium) in Fig. 2 are retained for comparison. For convenient reference, we add the physical parameters with units of F_A and Δl on the right and top sides of the diagram. At the last point before jump occurs, the black dot and cross mark are circled. Before the loading process, special care has to be taken to ensure that the metallic strip is well aligned between the two clamps, as shown in Fig. 12(a). In the loading process, there are three jumps as F_A increases from 0. The first jump occurs at $(F_A, \Delta l) = (1.431, 0.0003)$ when the strip buckles and contacts the wall at one point, as shown in Fig. 12(b). The second jump occurs at $(F_A, \Delta l) = (3.702, 0.0344)$ when the strip contacts the walls at two points, as shown in Fig. 12(c). The third jump occurs at $(F_A, \Delta l) = (6.622, 0.1348)$ when the strip contacts the walls at three points, as shown in Fig. 12(d). It is noted that the last two jumps are very close to the theoretical values at points g and k with discrepancy in F_A between theory and experiment being 0.2% and 5%, respectively.

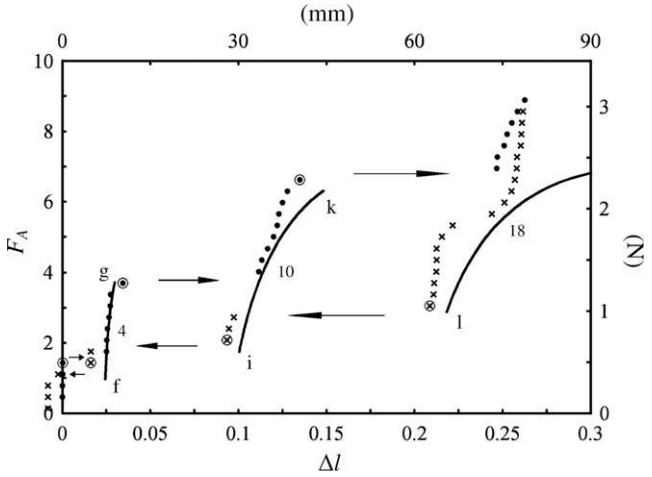

Fig. 11. Experimental results of the load–deflection relations. Black dots • and cross marks $\times$ are for loading and unloading processes, respectively.

After the third jump the strip deforms in a three-point contact pattern. The loading process stops at $F_A = 8.893$, and from then on the unloading process begins. The strip deformation jumps from three-point to two-point contact when $(F_A, \Delta l) = (3.053, 0.2087)$, and jumps from two-point to one-point contact when $(F_A, \Delta l) = (2.080, 0.0935)$, and finally jumps back to non-contact pattern when $(F_A, \Delta l) = (1.431, 0.0161)$. These three jumping loads are very close to the theoretical values at points l, i, and f, respectively. These observations from both the loading and unloading processes strongly suggest that the line-contact deformations 7-1 and 15-1 do not exist in the current experimental set-up.

The natural frequencies of the constrained elastica can be measured by using a photonic sensor (MTI-2000). The non-contact photonic probe shines a beam of light perpendicularly onto the surface of the strip at some point. The strip is hit by a small object simulating an impact. From the power spectrum of the response, which is collected and calculated with a spectrum analyzer, we can identify some of the lowest natural frequencies. The cross marks in Fig. 13 represent the first two measured natural frequencies of the one-point contact deformation (locus 4 in Fig. 2) in the loading process. Although the experimental results of the second natural frequency can go as much as 30% higher than the theoretical one, the trend that the two natural frequencies decrease toward zero as load increases is obvious.

The most difficult problem we faced in experimental observation is the friction in all the movable parts. For instance, the friction in the roller bearing simulating the feeding channel, the pulleys, and the sticky action between the metallic strip and the plane walls all contribute to the inaccuracy of the frequency measurement. In particular, it is assumed that sliding between the plane walls and the elastica must occur in the theory because friction is neglected. However, in reality, the sticky action due to the

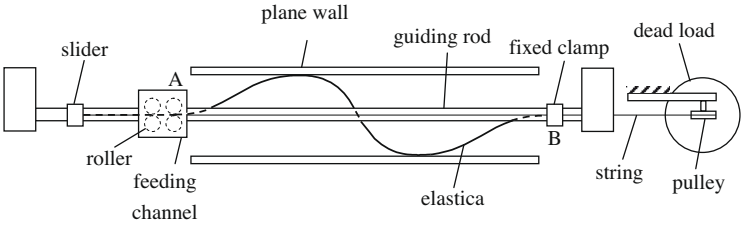

Fig. 10. Top view of the experimental set-up.

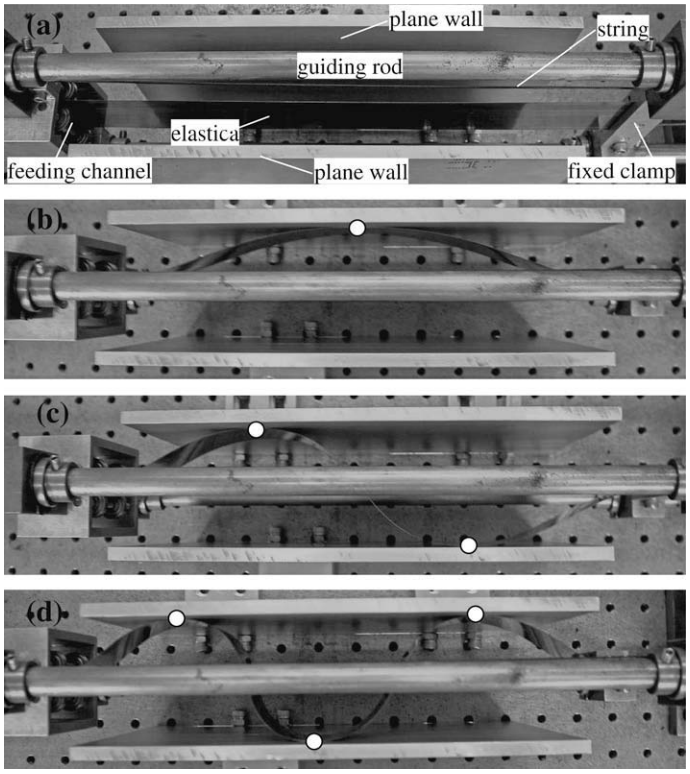

Fig. 12. Photographs of (a) straight configuration before Euler buckling, (b) one-point contact, (c) two-point contact, and (d) three-point contact deformations. The contact points are marked with white dots.

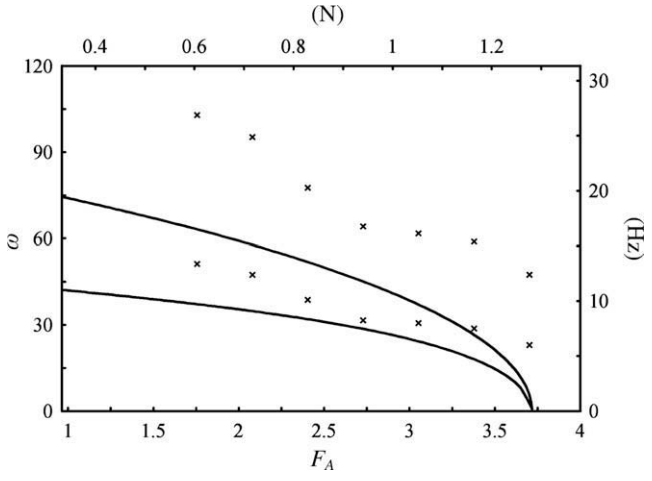

Fig. 13. The first two natural frequencies ω as functions of the edge thrust F_A for one-point contact deformation (locus 4 in Fig. 2). The cross marks $\times$ represent the experimental measurements.

friction between the walls and the elastica may prevent this type of sliding to occur. The situation deteriorates especially when the pushing force is large.

7. Comparison with previous works of others

One of the unique results reported in this paper is that none of the line-contact deformations exist in the experiment. The elastica is found to buckle far before reaching the secondary buckling load. However, several previous works on constrained elastica did observe line-contact deformations. One is the clamped–clamped elastica investigated by Chai (1998) and Roman and Pocheau (1999), and the other is the pinned–pinned elastica discussed by Domokos et al. (1997). It is noted that the elastica is of fixed length in these two cases. In this section, we confirm the validity of these previous investigations, both theoretically and experimentally, and propose explanations which may help us understand why the elasticas behave differently in different set-ups.

7.1. A clamped–clamped elastica

Chai (1998) and Roman and Pocheau (1999) conducted experiments on a clamped–clamped elastica and reported that line-contact deformations did exist and become unstable via secondary buckling. It is noted that the plane walls in these experiments are not symmetric with respect to the elastic strip. Instead, the walls are on $y = 0$ and h. We rearranged the experimental set-up in Fig. 10 by moving the plate on $y = -h$ to 0, a set-up similar to the experiments in Chai (1998) and Roman and Pocheau (1999). The measured load–deflection relations (F_A–Δl) are recorded in Fig. 14(a) with cross marks $\times$. The theoretical predictions are also drawn in Fig. 14(a) for comparison. The solid, dashed, and dotted lines represent stable, unstable, and neutral solutions from the vibration analysis.

We first compare the theoretical predictions on the load–deflection curves between Figs. 2 and 14(a). The one-point contact deformations 4 in Figs. 2 and 14(a) are the same. At point g deformation 4 evolves to line-contact deformation 7-1. In Fig. 2 a point on locus 7 (including 7-1 and 7-2) represents a single deformation. However, in Fig. 14(a) a point on locus 7 actually represents an infinite number of "similar" deformations. The line contact can occur on the upper wall, the base wall, or combined, as long as the sum of the lengths of the line-contact segments $\delta_1 + \delta_2 + \delta_3$ remains the same. This situation occurs in deformation 15 of Fig. 2 as well.

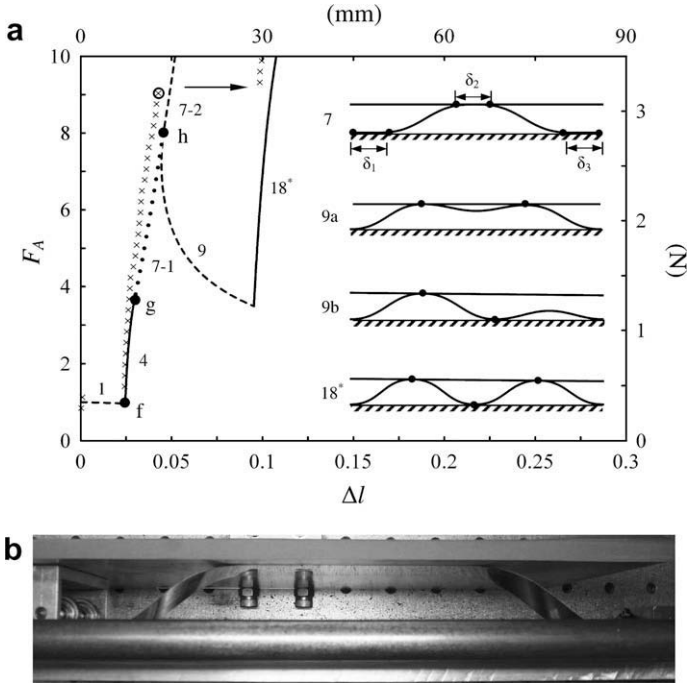

Fig. 14. (a) Experimental and theoretical results of the load–deflection relation when the plane walls are on $y = 0$ and h. (b) Photograph of the line-contact deformation.

The one-line contact deformation on locus 7 in Fig. 2 is a special case with $\delta_1 = \delta_3 = 0$. Furthermore, deformations 3 and 11 in Fig. 2 are prevented by the base plane wall and are absent in Fig. 14(a). As a result, there is no other "non-similar" deformation bifurcating away at point g. At point h locus 7-1 in Fig. 14(a) may bifurcate to locus 9. A point on locus 9 actually represents two different deformations 9a and 9b. In Fig. 2, on the other hand, only deformation 9a is possible. Locus 18* is a three-point contact deformation, which cannot be found in Fig. 2. Vibration analysis shows that the lowest two natural frequencies of any deformation on locus 7-1 in Fig. 14(a) are zero, the same result as in Fig. 2. Therefore, the stability of deformations on locus 7-1 remains inconclusive.

We next examine the experimental observation. It is clear that the elastica buckles at point h when F_A reaches the secondary buckling load. The line contact on the upper wall is clearly present, as shown in Fig. 14(b). It is baffling why the line-contact deformation on locus 7-1 of Fig. 14(a) can be observed, but the one in Fig. 2 cannot, in spite of the fact that the lowest two natural frequencies are degenerately zero in both cases. Several additional tests were conducted to find the cause of this difference. We first produced the line-contact deformation 7-1 in Fig. 14(b) and removed the base wall carefully. It was found that the strip snapped away immediately. Apparently, the base wall did do something in the line-contact deformation. Close inspection revealed that the strip actually touched the base wall symmetrically with very small segments. In other words, δ_1 and δ_3 are very small but not zero. We next used a digital video camera to record the dynamic buckling processes in both experiments. It was found that in Fig. 14(a) the elastica buckled at point h symmetrically via deformation 9(a). On the other hand, in Fig. 2 the elastica buckled at point g asymmetrically via deformation 3. Apparently, when and in what form the elastica buckles depend strongly on whether the load–deflection locus experiences a bifurcation. Based on these observations, we conjecture that for a constrained clamped–clamped elastica buckling may occur whenever a bifurcation is experienced in the process when it evolves from point- to line-contact deformations, such as points g and k in Fig. 2 and point h in Fig. 14(a).

7.2. A pinned–pinned elastica

Domokos et al. (1997) considered a pinned–pinned elastica constrained in the middle of a pair of plane walls, a symmetric set-up similar to the one discussed in this paper. One end of the elastica is under edge thrust F_A and is pushed in a distance. They observed that line-contact deformations did exist and become unstable via secondary buckling. The vibration analysis discussed in this paper can be applied to this case by properly modifying the boundary conditions. We assume that the pinned–pinned elastica is in two-point contact with the walls as shown in Fig. 15(a), a situation similar to the one in Fig. 1. During vibration the left end is moving back and forth with a small movement $\eta_0(t)$ in the form of Eq. (33). The exact boundary conditions at end A require that

$$M(s,t)|_{s=0} = \widehat{M}(\varepsilon_1,t)\Big|_{\varepsilon_1=-\eta_1} = 0 \tag{53}$$

$$x(s,t)|_{s=0} = \hat{x}(\varepsilon_1,t)|_{\varepsilon_1=-\eta_1} = \eta_0 \tag{54}$$

$$y(s,t)|_{s=0} = \hat{y}(\varepsilon_1,t)|_{\varepsilon_1=-\eta_1} = 0 \tag{55}$$

These boundary conditions can be linearized to the forms

$$\widehat{M}_d(\varepsilon_1)\Big|_{\varepsilon_1=0} = \left[F_{xe}(\varepsilon_1)|_{\varepsilon_1=0}\sin\theta_e(\varepsilon_1)|_{\varepsilon_1=0} - F_{ye}(\varepsilon_1)\Big|_{\varepsilon_1=0}\cos\theta_e(\varepsilon_1)|_{\varepsilon_1=0}\right]\eta_{1d} \tag{56}$$

$$\hat{x}_d(\varepsilon_1)|_{\varepsilon_1=0} = \eta_{0d} + \eta_{1d}\cos\theta_e(\varepsilon_1)|_{\varepsilon_1=0} \tag{57}$$

$$\hat{y}_d(\varepsilon_1)|_{\varepsilon_1=0} = \eta_{1d}\sin\theta_e(\varepsilon_1)|_{\varepsilon_1=0} \tag{58}$$

Similarly, the boundary conditions at end B can be linearized to the forms

$$\widehat{\widehat{M}}_d(\varepsilon_2)\Big|_{\varepsilon_1=0} = \left[F_{xe}(\varepsilon_2)|_{\varepsilon_2=1}\sin\theta_e(\varepsilon_2)|_{\varepsilon_2=1} - F_{ye}(\varepsilon_2)\Big|_{\varepsilon_2=1}\cos\theta_e(\varepsilon_2)|_{\varepsilon_2=1}\right]\eta_{2d} \tag{59}$$

$$\hat{\hat{x}}_d(\varepsilon_2)\Big|_{\varepsilon_2=1} = \eta_{2d}\cos\theta_e(\varepsilon_2)|_{\varepsilon_2=1} \tag{60}$$

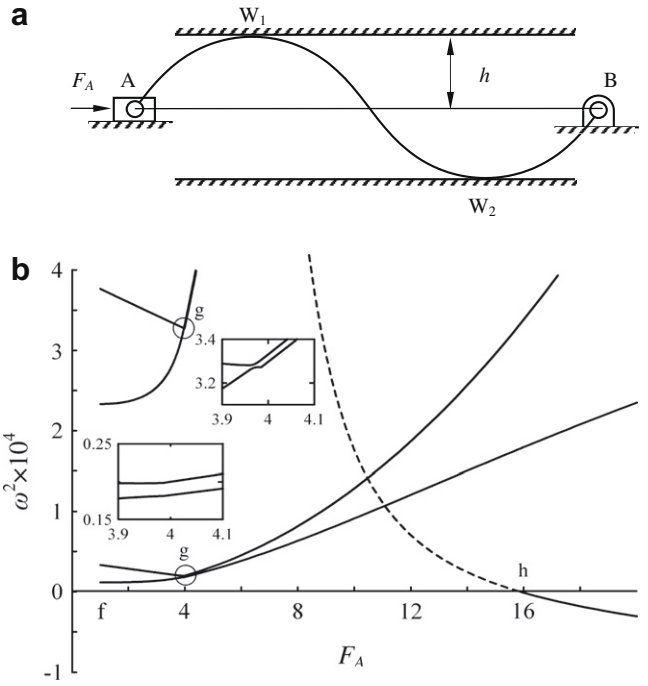

Fig. 15. (a) A pinned–pinned elastica constrained by a pair of plane walls. (b) ω^2 as functions of the edge thrust F_A when the pinned–pinned elastica ($h = 0.05$) evolves from one-point (f–g) to one-line (g–h) contact deformation. The line-contact deformation becomes unstable via secondary buckling at point h.

$$\hat{\dot{y}}_d(\varepsilon_2)\big|_{\varepsilon_2=1} = \eta_{2d}\sin\theta_e(\varepsilon_2)|_{\varepsilon_2=1} \tag{61}$$

The dynamic boundary condition F_A = constant yields Eq. (40), and the contact conditions at the contact points W_1 and W_2 remain the same as in Eqs. (44)–(49).

Fig. 15(b) shows the ω^2 as functions of F_A when the pinned–pinned elastica evolves from one-point to one-line contact. The gap $2h$ is set at 0.1, the same as in Domokos et al. (1997). Point f represents the start of one-point contact deformation. The deformation evolves from point contact to line contact at point g ($F_A = 3.984$), and becomes unstable via secondary buckling at point h ($F_A = 15.874$). The natural frequency loci near point g are magnified and shown in the two insets. It is noted that, unlike the clamped–clamped case discussed in this paper, there are no degenerately zero natural frequencies in line-contact deformations. This vibration analysis confirms that the line-contact deformation before secondary buckling is stable in the pinned–pinned elastica investigated by Domokos et al. (1997).

8. Conclusions

This paper studies the behavior of an elastica constrained by a pair of plane walls. One end of the elastica is fully clamped, while the other end is allowed to slide without friction and clearance inside a rigid channel. The elastica is compressed by a longitudinal force, causing it to buckle in the domain of interest between the full clamp and the opening of the feeding channel. As a consequence, the total length of the elastica between the two ends varies as the edge thrust increases. Both load-control and displacement-control procedures are discussed. Some of the conclusions can be summarized as follows.

(1) Static analysis allows us to find all the possible equilibrium configurations, including non-contact, point-contact, and line-contact deformations. In order to predict how the elastica behaves in reality, the stability of these equilibrium configurations needs to be determined. In this paper, a vibration method is adopted to calculate the natural frequencies and determine the stability of the constrained elastica.

(2) In order to take into account the sliding between the elastica and the plane constraints during vibration, Eulerian coordinates are defined to specify the positions of the material points on the elastica. After transforming the governing equations and the boundary conditions from the Lagrangian description to the Eulerian one, the natural frequencies and the mode shapes of the constrained elastica can be calculated. In line-contact deformations, the calculated mode shapes have to be discarded if they do not comply with the plane constraints.

(3) It is found that the lowest few natural frequencies approach and remain degenerately zero when point-contact deformations evolve to line-contact patterns. As a consequence, the stability of all line-contact deformations before secondary buckling cannot be determined from the linear vibration analysis.

(4) In order to observe what would happen in reality, a load-control experiment is conducted. It is found that the elastica jumps from one-point to two-point, and then to three-point contact with the walls without going through any line-contact deformations. These experimental observations are different from the results reported previously by others with different set-ups, in which line-contact deformations did exist. Explanations based on experimental evidences and theoretical analyses are provided to confirm the validity of these previous investigations and clarify the cause of the difference. It is conjectured that for a constrained clamped–clamped elastica buckling may occur whenever a bifurcation is experienced in the process when it evolves from point- to line-contact deformations.

References

Adan, N., Sheinman, I., Altus, E., 1994. Post-buckling behavior of beams under contact constraints. Journal of Applied Mechanics 61, 764–772.
Chai, H., 1998. The post-buckling behavior of a bilaterally constrained column. Journal of the Mechanics and Physics of Solids 46, 1155–1181.
Chai, H., 2002. On the post-buckling behavior of bilaterally constrained plates. International Journal of Solids and Structures 39, 2911–2926.
Chen, J.-S., Li, C.-W., 2007. Planar elastica inside a curved tube with clearance. International Journal of Solids and Structures 44, 6173–6186.
Chen, J.-S., Lin, Y.-Z., 2008. Snapping of a planar elastica with fixed end slopes. Journal of Applied Mechanics 75, 041024.
Chen, J.-S., Ro, W.-C., 2010. Deformations and stability of an elastica subjected to an off-axis point constraint. Journal of Applied Mechanics 77, 031006.
Domokos, G., Holmes, P., Royce, B., 1997. Constrained Euler buckling. Journal of Nonlinear Science 7, 281–314.
Feodosyev, V.I., 1977. Selected Problems and Questions in Strength of Materials. Mir, Moscow. Translated from the Russian by M. Konyaeva.
Holmes, P., Domokos, G., Schmitt, J., Szeberenyi, I., 1999. Constrained Euler buckling: an interplay of computation and analysis. Computer Methods in Applied Mechanics and Engineering 170, 175–207.
Kanno, Y., Ohsaki, M., 2009. Optimization-based stability analysis of structures under unilateral constraints. International Journal of Numerical Methods in Engineering 77, 90–125.
Klarbring, A., 1988. On discrete and discretized non-linear elastic structures in unilateral contact (stability, uniqueness and variational principles). International Journal of Solids and Structures 24, 459–479.
Kuru, E., Martinez, A., Miska, S., Qiu, W., 2000. The buckling behavior of pipes and its influence on the axial force transfer in directional wells. ASME Journal of Energy Resources Technology 122, 129–135.
Lu, Z.-H., Chen, J.-S., 2008. Deformations of a clamped–clamped elastica inside a circular channel with clearance. International Journal of Solids and Structures 45, 2470–2492.
Roman, B., Pocheau, A., 1999. Buckling cascade of thin plates: forms, constraints and similarity. Europhysics Letters 46, 602–608.
Roman, B., Pocheau, A., 2002. Post-buckling of bilaterally constrained rectangular thin plates. Journal of the Mechanics and Physics of Solids 50, 2379–2401.
Rumyantsev, V.V., 2006. Variational principles for systems with unilateral constraints. Journal of Applied Mathematics and Mechanics 70, 808–818.

Santillan, S.T., Virgin, L.N., Plaut, R.H., 2006. Post-buckling and vibration of heavy beam on horizontal or inclined rigid foundation. Journal of Applied Mechanics 73, 664–671.

Schulz, M., Pellegrino, S., 2000. Equilibrium paths of mechanical systems with unilateral constraints I. Theory. Proceedings of the Royal Society of London, Series A 456, 2223–2242.

Tschope, H., Onate, E., Wriggers, P., 2003. Direct computation of instability points for contact problems. Computational Mechanics 31, 173–178.

Villaggio, P., 1979. Buckling under unilateral constraints. International Journal of Solids and Structures 15, 193–201.

Wang, C.M., Lam, K.Y., He, X.Q., 1998. Instability of variable-arc-length elastica under follower force. Mechanics Research Communications 25, 189–194.